Check for updates

Optical Metrology of Critical Dimensions in Large-Area Nanostructure Arrays With Complex Patterns

Ramin Sabbagh[1]
Walker Department of Mechanical Engineering,
The University of Texas at Austin,
Austin, TX 78712
e-mail: sabbagh@utexas.edu

Alec Stothert
MathWorks,
Natick, MA 01760
e-mail: astother@mathworks.com

S. V. Sreenivasan
Walker Department of Mechanical Engineering,
The University of Texas at Austin,
Austin, TX 78712
e-mail: sv.sreeni@mail.utexas.edu

Dragan Djurdjanovic
Walker Department of Mechanical Engineering,
The University of Texas at Austin,
Austin, TX 78712
e-mail: dragand@me.utexas.edu

It was recently demonstrated that scatterometry-based metrology has the capability to perform high-throughput metrology on large-area nanopatterned surfaces. However, the way this approach is currently pursued requires an a priori generated library of reflectance spectra to be simulated for an exhaustive set of possible underlying critical dimensions (CDs) characterizing the measured nanopatterns. Generating this library is time consuming and can be infeasible for complex patterns characterized by a large number of CDs. This article addresses the aforementioned drawback of optical inspection of CDs of nanopatterned surfaces through the use of an inverse problem-based optimization methodology coupled with a recently introduced approach for efficient organization of the library of previously simulated reflectance spectra. Specifically, for each physically measured reflectance spectrum, the best matching simulated spectrum is sought in the initial incomplete library in order to serve as the initial guess for the inverse problem optimization process. Through that optimization process, further refinements of the best matching simulated spectra are conducted to obtain sufficiently accurate estimates of the CDs characterizing the inspected nanopattern geometries. Capabilities of the newly proposed approach are evaluated through inspection of semiconductor wafer samples with hourglass patterns characterized by eight CDs. It was observed that one can obtain significantly faster measurements of CDs compared to inspection times associated with scanning electron microscopy, while at the same time not deteriorating the corresponding Gage Repeatability and Reproducibility. In conclusion, this method enables real-time, accurate, and repeatable metrology of CDs of large-area nanostructured surfaces with complex nanopatterns.
[DOI: 10.1115/1.4056923]

Keywords: real-time metrology, critical dimensions of nanopatterned surfaces, inverse problems, organization and search of metrology data, inspection and quality control, metrology, modeling and simulation, sensing, monitoring and diagnostics

Downloaded from http://nuclearengineering.asmedigitalcollection.asme.org/manufacturingscience/article-pdf/145/6/061010/6995189/manu_145_6_061010.pdf by guest on 16 August 2024

1. Introduction

Over the last couple of decades, unique optical properties of nanophotonic structures have brought the promise of exciting new technologies such as high-speed lossless communications, diffractive optics, photonic crystals, negative index-of-refraction materials, flat lenses, perfect reflectors, perfect absorbers, and cloaking devices [1–3]. Today, a deeper understanding of the physics behind nanophotonics phenomena, coupled with advancements in nano-fabrication techniques, has facilitated the pursuit of industrial-scale manufacturing of products that could realize some of these exciting capabilities. In particular, modern high-throughput nanopatterning techniques, such as nanoimprint lithography [4], have enabled fabrication of large-area nanostructure arrays (LNAs) on wafers and roll-to-roll substrates reaching scales as large as cm^2 or m^2. The capability to manufacture such LNAs on a variety of substrates, including silicon wafers, glass sheets, and flexible roll-to-roll webs, has enabled design and manufacturing of a wide array of products, including optical devices such as wire-grid polarizers [5], transparent conductors [6], color filters [7], and anti-reflection surfaces [8], as well as building blocks for electronic components, such as ultra-capacitors [9], optical sensors [10], and memory storage architectures [11].

A significant challenge associated with scaling up manufacturing of nanopatterned surfaces is the fact that traditional metrology methods, such as microscopy or point-to-point scatterometry-based inspections, are not amenable to high manufacturing throughput. For instance, nanoscale microscopy-based metrology techniques, such as scanning electron microscopy (SEM) [12] or atomic force microscopy [13], directly measure the geometric parameters, or the so-called critical dimensions (CDs) characterizing LNA nano-features. Consequently, those approaches have prohibitively small fields of view,[2] which makes microscopy-based solutions unsuitable for metrology in such processes. Furthermore, obtaining three-dimensional measurements often requires sample destruction, as is the case with cross-sectional SEM-based metrology [15], which further hinders the existing inspection methods.

State-of-the-art alternatives for microscopy-based inspection methods are reflectance-based optical scatterometry metrology techniques, namely, ellipsometric scatterometry and angular scatterometry methods. Both methods are nondestructive, nanoscale, and noncontact inspection methods that are based on reflectance of light obtained from periodic nanostructures fabricated on large-area nano-surfaces. In ellipsometric scatterometry, the angle of incidence is fixed, and the wavelength is varied. However, in angular scatterometry, the angle of incidence is varied, while a fixed wavelength source, usually a high brightness laser source, is

[1]Corresponding author.
Manuscript received November 15, 2022; final manuscript received January 30, 2023; published online March 14, 2023. Assoc. Editor: Cheryl Xu.

[2]Micron scale or smaller, which is significantly smaller than what is needed for metrology of cm^2 or m^2 nanostructure arrays [14].

Copyright © 2023 by ASME

used [16,17]. Both techniques have demonstrated resolution to feature sizes relevant to advanced manufacturing needs and have their own advantages compared to each other [18].[3]

Even though optical scatterometry-based inspection methods allow for nondestructive geometric characterization with speeds higher than those associated with microscopy-based approaches,[4] the corresponding field of view is still a severe limiting factor for manufacturing throughput due to their point-to-point measurement nature. Furthermore, when scatterometry-based inspection of nanopatterned surfaces is pursued, a library of reflectance spectra corresponding to an exhaustive set of possible CDs characterizing the measured nanopatterned surface needs to be constructed a priori [14] using simulations grounded in first-principle physics-based methods, such as rigorous coupled wave analysis [21] or finite difference time domain (FDTD) approaches [22]. During the metrology process, for any reflectance spectrum acquired during inspection of a nanopatterned surface, the corresponding CDs are inferred by finding in the simulated library of reflectance spectra the spectrum that is nearest to the measured spectrum, and associating parameters of the inspected surface area with the corresponding parameters in the library.

In summary, the scatterometry-based metrology process described earlier essentially consists of three stages: (1) offline creation of the library of simulated reflectance spectra based on which CDs of the measured nanopatterned surface can be inferred, (2) acquisition of experimental reflectance spectra from the nanopatterned surface that is being measured, and (3) search within the created library of reflectance spectra to identify the spectrum that best matches the measured spectrum. Each of these stages is associated with challenges when it comes to the need to perform them quickly.

The measurement acquisition stage of the scatterometry-based metrology concept has been significantly accelerated via parallelization of acquisition of reflectance spectra described in Ref. [14]. Specifically, Gawlik et al. [14] introduced a hyperspectral imaging system that enabled a 19 mm-by-23 mm field of view, within which each of the nearly 5-million μm scale pixels acted as a receiver of scattered light spectra [11,19].

The library search stage of the earlier described metrology concept has also been recently improved utilizing a tree-structured database organization realized through the use of distance-based unsupervised clustering [23,24]. Specifically, a growing self-organizing map was used to parse the library of spectral data into clusters of similar spectra, each of which is represented by a centroid weight vector, with the resulting Voronoi tessellation naturally providing boundaries between clusters [25]. Within a thus-organized library, a search for the spectrum that is the closest to any given experimentally acquired spectrum can be performed hierarchically, by first identifying the cluster of spectra whose representative weight vector is the closest to the query spectrum, after which best matches can be pursued inside that cluster alone, rather than the entire library. The use of the aforementioned tree-based databased organization enables logarithmic acceleration in database searches [26,27], which led to dramatic improvements in times needed to obtain reflectance spectra-based measurements without any deterioration in metrology accuracy [23,24].

Unfortunately, challenges associated with the library creation stage have not been addressed and will be tackled in this article. Specifically, when it comes to even slightly more complex nanostructures than the ones analyzed in Ref. [23], such as wineglass or inverted hourglass patterns,[5] creation of an exhaustive library of reflectance spectra simulated for all possible values of the underlying CDs cannot be done with sufficient resolution. For instance, if one is measuring a nanopatterned wafer with hourglass-shaped

[3]The methodology proposed in this article is applied on an ellipsometric optical metrology system, the so-called hyperspectral imaging system, but it is general enough to be applicable to angular metrology systems as well.

[4]This is due to their larger field of view (hundreds of micrometers to millimeter scale) compared to microscopy-based inspection methods [19,20].

[5]That is, patterns characterized by more than five CDs.

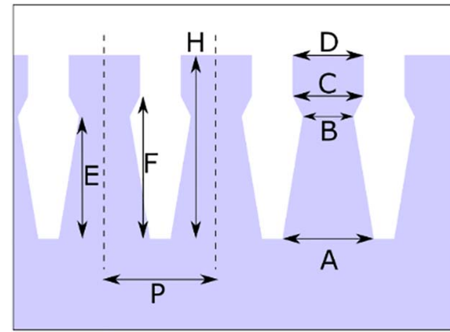

Fig. 1 Illustration of hourglass-shaped patterns and their critical dimensions

structures characterized by eight CDs, as illustrated in Fig. 1, creation of a library with a resolution of ten steps per parameter[6] implies the need to perform 10^8 physics-based simulations. Considering that currently each simulation takes about 20 s to perform on a standard PC, creation of such a library would take over 60 years.

Obviously, brute force generation of an exhaustive library of spectra is not an option for complex nanopatterns. In this article, we will address this gap by more strategically generating entries for the library of simulated reflectance spectra based on which CDs of the underlying nanopatterned surface will be inferred. The method starts with a sparse, incomplete library of spectrum templates, which can be generated offline. For each experimentally measured reflectance spectrum, this library will be searched to identify its best match. The CDs associated with that best match will be used as the initial guess for the inverse problem optimization process via which further refinement of the simulated reflectance spectra will be pursued to obtain sufficiently accurate estimates of the underlying CDs. Furthermore, reflectance spectra simulated during execution of the inverse problem will be added to the initial library, thus enriching it and providing potentially better initial guesses for future inverse problems.

More details on the earlier described procedure are offered in the remainder of this article, which is organized as follows. In Sec. 2, the concept of inverse problems will be coupled with the recently introduced approach for efficient organization of metrology databases to enable optical metrology of CDs characterizing complex nanoscale patterns. In Sec. 3, inspection speed and Gage Repeatability and Reproducibility (Gage R&R) [28] of the newly proposed method will be evaluated on semiconductor wafer samples with hourglass patterns. Finally, conclusions of the research reported in this article, as well as several directions for potential future explorations will be discussed in Sec. 4.

2 Methodology

In this article, we utilize an inverse problem optimization method to enable optical metrology of CDs for large-area nanostructure arrays with complex patterns. An inverse problem in science can be seen as the process of calculating from a set of observations the causal factors that produced them [29]. Inverse problems are some of the most important problems in science and mathematics because they are used to determine parameters that one cannot directly observe or observing them is expensive [30,31], which is the case in optical metrology. Inverse problems have wide array of applications in geoscience [32,33], weather forecasting [34], oceanography [35], medical imaging [36,37], chemistry [38,39], biology [40], pharmaceutical industries [41], machine learning

[6]One should note that this resolution is not very dense, and in reality, even denser grid of CDs would be needed.

Downloaded from http://nuclearengineering.asmedigitalcollection.asme.org/manufacturingscience/article-pdf/145/6/061010/6995189/manu_145_6_061010.pdf by guest on 16 August 2024

(ML) [42,43], computer vision [44,45], nondestructive testing [46], and many other fields.

In this article, we postulate the inverse problem in a way that inputs are sets of values of CDs characterizing nanostructures, while outputs are the corresponding simulated reflectance spectra values evaluated on the grid of wavelengths at which the inspection device is collecting reflectance spectra. The simulations can be performed utilizing LUMERICAL software,[7] which solves Maxwell's equations [47] using the FDTD method [22]. Each simulation can be formulated as follows:

$$F(\boldsymbol{x}) = R(\lambda) \in \mathbb{R}^{m} \tag{1}$$

where $R(\lambda)$ is an m-dimensional reflectance spectrum associated with the vector $\boldsymbol{x} \in \mathbb{R}^n$ of CDs, $\mathcal{F}$ is the simulation function, m is the number of wavelengths at which the simulated reflectance spectrum is obtained, and n is the number of CDs characterizing the nanopatterns fabricated on the inspected wafers. One should note that evaluation of the function $\mathcal{F}(\boldsymbol{x})$ is often referred to as the forward problem [29].

The objective function for the inverse problem in this article is to find the set of CDs that minimizes the distance between an experimentally obtained reflectance curve d obtained via hyperspectral imaging[8] from a target pixel area on the inspected surface [14] and the simulated reflectance curve $\mathcal{F}(\boldsymbol{x})$. More formally,

$$\boldsymbol{x}^* = \arg\min_{\boldsymbol{x}} J(\boldsymbol{x}) = \arg\min_{\boldsymbol{x}} ||\mathcal{F}(\boldsymbol{x}) - d||^2 \tag{2}$$

Since the forward problem $\mathcal{F}(\boldsymbol{x})$ does not have a tractable analytical formulation, one of the challenges in the simulation-based optimization problem (2) is the need to analytically calculate the gradients at different locations of the domain $\boldsymbol{x}$. A natural way to evaluate gradients is to use finite difference methods [48], which can be time consuming, especially for problems where performing each simulation is computationally expensive and/or there are a lot of parameters in the optimization problem. Assuming there are 8 parameters, like in the case of hourglass patterns, each full gradient evaluation using central finite differences would require 16 executions of FDTD simulations,[9] which is computationally demanding. Furthermore, calculating Hessians using finite difference methods is even more computationally expensive[10] and, in addition, may not be accurate [49,50]. Thus, traditional gradient-descent based optimization algorithms, or optimization approaches that utilize exact Hessians, such as Newton's method [51], are not efficient methods for simulation-based optimization problems, such as (2). Instead, in this article, we propose the use of a hybrid, Quasi Newton optimization method [52] for solving (2). This method relies on evaluating the gradients based on the so-called deterministic-stochastic hill climbing method, which can be seen as an extension to the hill climbing method [53], and approximating the Hessian via Broyden–Fletcher–Goldfarb–Shanno (BFGS) update [54–57].

In order to evaluate the gradient, we conduct a sensitivity analysis following Ref. [58] and determine the influence of each CD on the output defined by Eq. (1). We include the top three most influential CDs identified by sensitivity analysis to be in the gradient and then randomly choose one more CD from the remaining parameters.[11] For instance, assuming that the top three most influential parameters are $\boldsymbol{x}_2$, $\boldsymbol{x}_3$, and $\boldsymbol{x}_6$, and the randomly selected parameter is $\boldsymbol{x}_7$, the gradient will be approximated as follows:

$$\nabla J(\boldsymbol{x}) = \left[\frac{\partial J(\boldsymbol{x})}{\partial \boldsymbol{x}_1}, \frac{\partial J(\boldsymbol{x})}{\partial \boldsymbol{x}_2}, \frac{\partial J(\boldsymbol{x})}{\partial \boldsymbol{x}_3}, \frac{\partial J(\boldsymbol{x})}{\partial \boldsymbol{x}_4}, \frac{\partial J(\boldsymbol{x})}{\partial \boldsymbol{x}_5}, \frac{\partial J(\boldsymbol{x})}{\partial \boldsymbol{x}_6}, \frac{\partial J(\boldsymbol{x})}{\partial \boldsymbol{x}_7}, \frac{\partial J(\boldsymbol{x})}{\partial \boldsymbol{x}_8}\right] \approx \left[0, \frac{\partial J(\boldsymbol{x})}{\partial \boldsymbol{x}_2}, \frac{\partial J(\boldsymbol{x})}{\partial \boldsymbol{x}_3}, 0, 0, \frac{\partial J(\boldsymbol{x})}{\partial \boldsymbol{x}_6}, \frac{\partial J(\boldsymbol{x})}{\partial \boldsymbol{x}_7}, 0\right] \tag{3}$$

where each nonzero component of the gradient approximation is calculated using the well-known central finite difference method.

$$\frac{\partial J(\boldsymbol{x})}{\partial \boldsymbol{x}_i} = \frac{J(\boldsymbol{x}_1, \boldsymbol{x}_2, \ldots, \boldsymbol{x}_i + \delta_i, \ldots, \boldsymbol{x}_n) - J(\boldsymbol{x}_1, \boldsymbol{x}_2, \ldots, \boldsymbol{x}_i - \delta_i, \ldots, \boldsymbol{x}_n)}{2\,\delta_i} \tag{4}$$

The BFGS method for approximating the inverse of the Hessian matrix takes advantage of a special case of the Sherman–Morrison–Woodbury method [59] to provide an update for inverse of the Hessian approximation, thus avoiding the complications of matrix inversions and long multiplications in each step. More precisely, the BFGS approximation for the inverse Hessian $\nabla^2 \boldsymbol{J}(\boldsymbol{x})^{-1}$ is obtained as follows:

$$\nabla^2 J(\boldsymbol{x}^{k+1})^{-1} \approx \mathbf{H}^{k+1} = \left(\mathbf{I} - \frac{\boldsymbol{s}^k \boldsymbol{y}^{kT}}{\boldsymbol{y}^{kT}\boldsymbol{s}^k}\right)\mathbf{H}^k\left(\mathbf{I} - \frac{\boldsymbol{y}^k \boldsymbol{s}^{kT}}{\boldsymbol{y}^{kT}\boldsymbol{s}^k}\right) + \frac{\boldsymbol{s}^k \boldsymbol{s}^{kT}}{\boldsymbol{y}^{kT}\boldsymbol{s}^k} \tag{5}$$

where $\boldsymbol{s}^k = \boldsymbol{x}^{k+1} - \boldsymbol{x}^k$, $\mathbf{y}^k = \nabla J(\boldsymbol{x}^{k+1}) - \nabla J(\boldsymbol{x}^k)$, $\mathbf{H}^k$ is the approximation of the inverse Hessian $\nabla^2 J(\boldsymbol{x}^k)^{-1}$ calculated using the BFGS method (5), and k is the optimization iteration.[12]

Optimization direction $\boldsymbol{p}$ is evaluated by solving $\nabla^2 J(\boldsymbol{x}^k)^{-1}\, \boldsymbol{p}^k = -\nabla J(\boldsymbol{x}^k)$ and is calculated as follows:

$$\boldsymbol{p}^k = -\nabla^2 J(\boldsymbol{x}^k)^{-1}\, \nabla J(\boldsymbol{x}^k) \approx -\mathbf{H}^k\, \nabla J(\boldsymbol{x}^k) \tag{6}$$

where $\nabla J(\boldsymbol{x})$ denotes the gradient at location x approximated based on the earlier-mentioned deterministic-stochastic hill climbing method.

In order to make sure that the optimization step size is of the appropriate size, Wolfe conditions were used [60]. Specifically, for any choice of constants α_1 and α_2 satisfying

$$0 < \alpha_1 < \alpha_2 < 1 \tag{7}$$

the optimization step t is chosen via backtracking such that it satisfies the following constraints:

$$f(\boldsymbol{x}^k + t\boldsymbol{p}^k) \le f(\boldsymbol{x}^k) + \alpha_1 t\, \nabla f(\boldsymbol{x}^k)^T \boldsymbol{p}^k \tag{8}$$

$$\nabla f(\boldsymbol{x}^k + t\boldsymbol{p}^k)^T \boldsymbol{p}^k \ge \alpha_2\, t\, |\nabla f(\boldsymbol{x}^k)^T \boldsymbol{p}^k| \tag{9}$$

[7] https://www.lumerical.com/products/fdtd/

[8] More details on experimental measurements are provided in the Appendix section.

[9] Each FDTD simulation using LUMERICAL software takes about 20 s on a standard PC.

[10] For the case involving eight CDs, such as the case of hourglass nanopatterns, calculating each Hessian using central difference requires 32 simulations.

[11] The number of included CDs in the gradient is empirically chosen and can be changed depending on nanostructure's shape, availability of computational power, availability of time, etc. Our goal is to choose as few CDs as possible such that we do not lose significant amount of information evaluated by sensitivity analysis described in Ref. [13]. There are many alternative importance scoring methods such as [65–67], which can be utilized to obtain an optimally down-selected set of CDs for the inverse problem.

[12] The BFGS update satisfies the following requirements known as Broyden's family of requirements [4]. (1) $\mathbf{H}^{k+1}$ satisfies the secant equation $\mathbf{H}^{k+1}\, \boldsymbol{y}^k = \boldsymbol{s}^k$. The idea behind the secant equation is to use the information in $\mathbf{H}^k$ to calculate $\mathbf{H}^{k+1}$ instead of calculating it from the scratch. (2) $\mathbf{H}^{k+1}$ is symmetric. (3) $\mathbf{H}^{k+1}$ is close to $\mathbf{H}^k$. (4) If $\mathbf{H}^k$ is positive definite, then $\mathbf{H}^{k+1}$ is also positive definite. Thus, if the Hessian is initialized by an arbitrary positive definite matrix of an appropriate size (i.e., identity matrix), $\mathbf{H}^{k+1}$ will remain positive definite in all of the future iterations.

Downloaded from http://nuclearengineering.asmedigitalcollection.asme.org/manufacturingscience/article-pdf/145/6/061010/6995189/manu_145_6_061010.pdf by guest on 16 August 2024

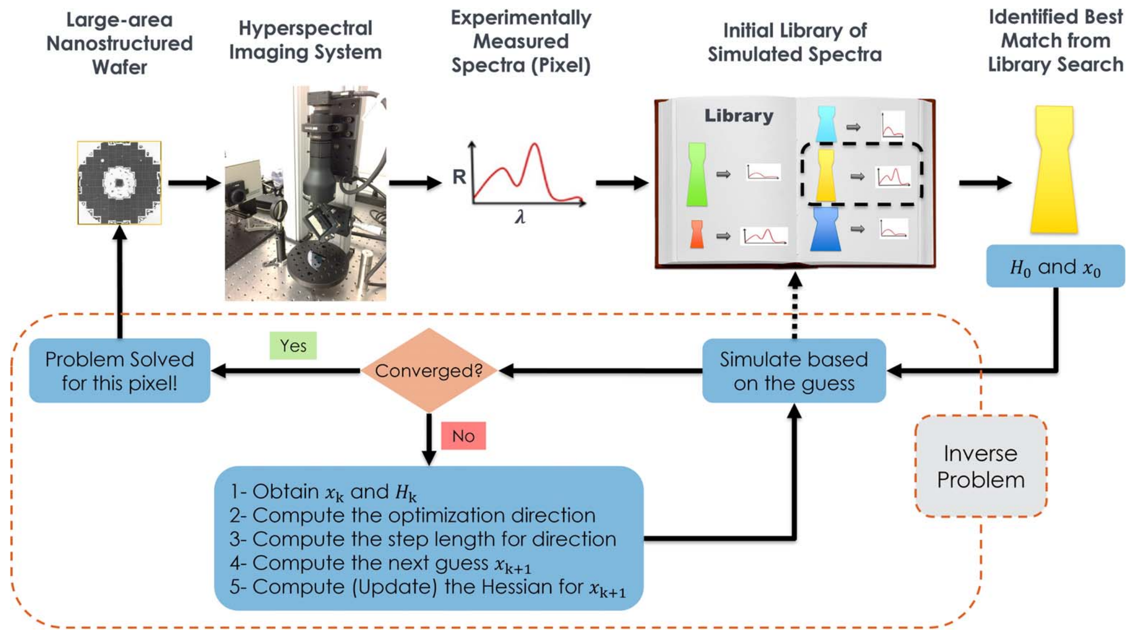

Fig. 2 High-level illustration of the inverse problem-based method for metrology of CDs of complex nanoscale patterns using reflectance spectra

Once the optimization direction and the step size are calculated, the next location of $\boldsymbol{x}$ is obtained as follows:

$$\boldsymbol{x}^{k+1} = \boldsymbol{x}^k + t^k \boldsymbol{p}^k \tag{10}$$

where k is the iteration number, $\boldsymbol{p}$ is the optimization direction, and t^k is the final optimization step in iteration k satisfying the Wolfe conditions (8) and (9).

We iterate through the inverse problem stage of the proposed method until the final simulated reflectance spectrum is sufficiently close to the experimentally acquired reflectance spectrum, as per some predefined distance threshold. The CDs associated with that final simulation are then identified as the final estimated CDs for that specific target pixel area.

In order to provide initial guesses for the inverse problems and limit the number of iterations that need to be run, an initial library of reflectance spectra is created through simulations performed using a sparse, incomplete grid of CDs characterizing the inspected nanopattern.[13] This initial library can be built by specifying a start, an end, and a (typically large) resolution value for each of the CDs. The offline generated initial library was organized utilizing methods proposed in Ref. [23] in order to enable fast and accurate findings of the simulated spectrum that best matches any given experimentally acquired reflectance spectrum. The CDs associated with the best match from the initial library were then used as the initial guess for the inverse problem (2) via which sufficiently accurate estimates of the CDs associated with inspected pixel area are obtained. A high-level illustration for the proposed method is shown in Fig. 2.

Another element of the proposed method that improved the speed of determining CDs of nanopatterns based on measured reflectance spectra was the continuous library enrichment with each simulation conducted during the inverse problem optimization. As illustrated by the dashed arrow in Fig. 2, results of simulations conducted during solution of the inverse problem (2) are continuously added into the library of simulated spectra, which means that the library grows and becomes richer as one solves inverse problems for more and more measured reflectance spectra. For example, with each iteration, calculating gradient results with addition of eight simulated spectra into the library, each check of the Wolfe conditions for step length adds at least 16 spectra into the library of simulated spectra, and finally, moving to the next location adds one more simulated spectrum into the library. Consequently, as more and more inverse problems are solved to infer CDs corresponding to more and more reflectance spectra, the initial best match from the library of reflectance spectra may often end up providing sufficiently accurate CD estimation and thus eliminates the need to perform inverse problem.

In order to formally assess capabilities of the newly proposed method for inspection of CDs of nanopatterned surfaces, its Gage R&R[14] [35] was formally evaluated and compared to that of SEM-based metrology, whose accuracy and precision are considered adequate for this metrology task [61].[15] In this article, a standard Gage R&R procedure described in Ref. [28] was utilized, with two participating operators, five parts (i.e., pixel areas), and three repetition trials, meaning that for a specific part and a specific operator, we measure the same reflectance spectrum-related pixel area three times. We evaluate repeatability, reproducibility, and Gage R&R ratios for each CD of the underlying pattern separately.[16]

3 Result

The newly proposed methodology for optical inspection of CDs in complex nanostructures was evaluated on multiple semiconductor wafer samples with nanoscale hourglass patterns. Figure 3 illustrates inspection results from one such wafer sample with hourglass patterns. The CD values shown in Fig. 3(*d*) are obtained as average measurements of ten different hourglass features in multiple locations in the same sample, as estimated using IMAGEJ software [62].

In order to provide an initial guess for the inverse problem, an initial library was generated offline by simulating reflectance spectra for an incomplete, but computationally feasible set of CDs

[13]The initial library creation should be feasible and not time consuming, considering the available time and computational resources.

[14]Gage R&R is defined as the process used to evaluate a gaging instrument's accuracy by ensuring that its measurements are repeatable and reproducible. The process includes taking a series of measurements to certify that the same measurements are obtained under the same operating conditions over a set duration.

[15]Though, as mentioned earlier, it is considerably too slow for real-time metrology of CDs of nanopatterns.

[16]Thus, for the inverse hourglass structure, we will have eight different Gage R&R ratios – one for each critical dimension.

Downloaded from http://nuclearengineering.asmedigitalcollection.asme.org/manufacturingscience/article-pdf/145/6/061010/6995189/manu_145_6_061010.pdf by guest on 16 August 2024

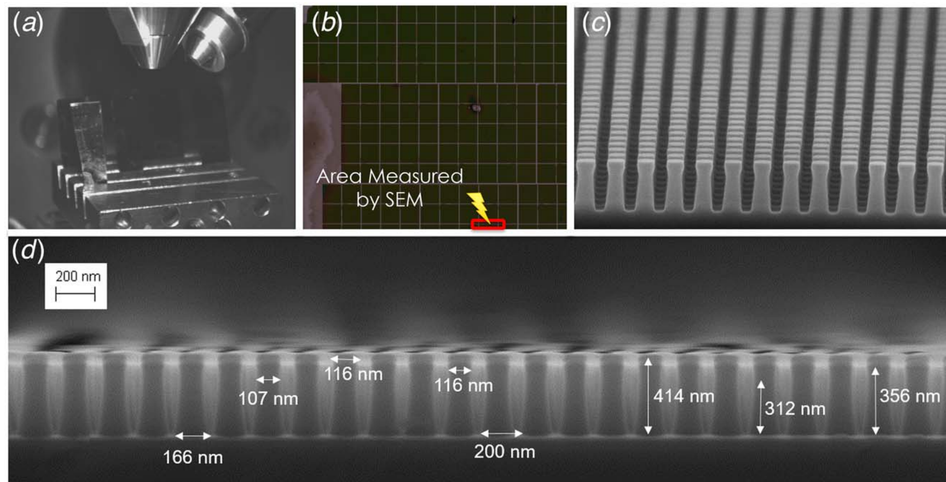

Fig. 3 (*a*) Picture of different hourglass wafer samples taken from inside of the ZEISS SEM. (*b*) RGB image of a wafer sample with hourglass patterns captured by the hyperspectral imaging system (c) A 70-deg picture from cross section of the area of the hourglass wafer sample specified with red rectangle in (*b*) taken by ZEISS SEM. (*d*) A right-angle picture from cross section of the area specified with red rectangle in (*b*) as well as measured CD values.

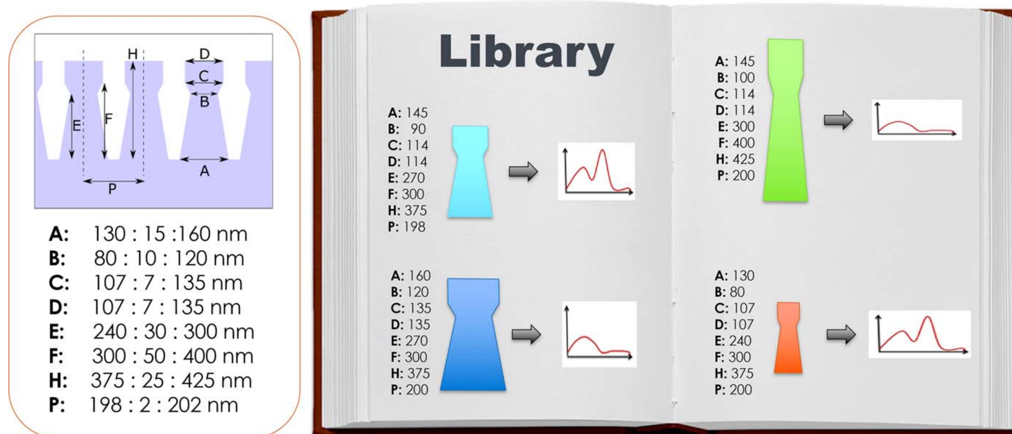

Fig. 4 Illustration of initial library creation with respect to different values of hourglass CDs

characterizing hourglass nanopatterns. Specifically, reflectance spectra are simulated for a grid of values of parameters A, B, C, D, E, F, H, and P illustrated in Fig. 4, with that grid being defined based on the start, end, and resolution values for each parameter, which are also shown in Fig. 4. Such combinations resulted in over 30,000 simulations. Considering that each lumerical simulation of reflectance spectra for wavelengths of 400–700 nm with steps of 5 nm took about 20 s on a standard PC, the entire library generation took about 10 days.[17] Following Ref. [23], this library was then organized into clusters of similar reflectance spectra in order to enable fast and efficient searches within it. The library organization process took about 90 min on a standard PC.

In order to evaluate a gradient based on the proposed stochastic-deterministic hill climbing method, a sensitivity analysis was conducted on the initial library of spectra, and the parameters D, H, and B were identified as the most influential CDs affecting the reflectance spectra simulations. Following a standard procedure [63], we initialized the inverse Hessian approximation with an identity matrix and updated it via the proposed BFGS method (5). Figure 5 shows a result of matching one reflectance spectrum obtained from the semiconductor wafer shown in Fig. 3 with simulated reflectance spectra, based on which the underlying CDs could be inferred. Fig. 3(*a*) shows the best match obtained from the offline generated library, while Fig. 3(*b*) shows the best match obtained using the newly proposed inverse problem-based methodology, with the initial guess being the best match from the offline generated library.[18] One can notice that the use of the inverse problem-based optimization clearly provided a much better match between the theoretical and experimentally obtained spectra. It took the inverse problem-based optimization 68 iterations to converge and yield the improved match shown in Fig. 5.

CD measurements estimated from the experimental reflectance spectrum shown in Fig. 5 are summarized in Table 1, alongside the corresponding SEM measurements obtained from the same area (specified with a yellow arrow inside the red rectangle in Fig. 3). The reason behind choosing this area to compare the proposed metrology method against the SEM-based approach is the fact that the SEM is only able to measure 3D structures by cross sectioning a wafer and inspecting patterns on the edge of the cut wafer samples. It is unable to measure areas in the middle sections of the wafer samples—this is one of the main motivations of pursuing alternative metrology approaches, such as the one considered in this article. One can observe that the use of the inverse

[17]Please note that this initial library could have been generated to be even smaller, using even sparser combinations of CDs, if the limitations of time, computational power, and other relevant resources were more stringent.

[18]That best match is shown in Fig. 3(*a*).

Downloaded from http://nuclearengineering.asmedigitalcollection.asme.org/manufacturingscience/article-pdf/145/6/061010/6995189/manu_145_6_061010.pdf by guest on 16 August 2024

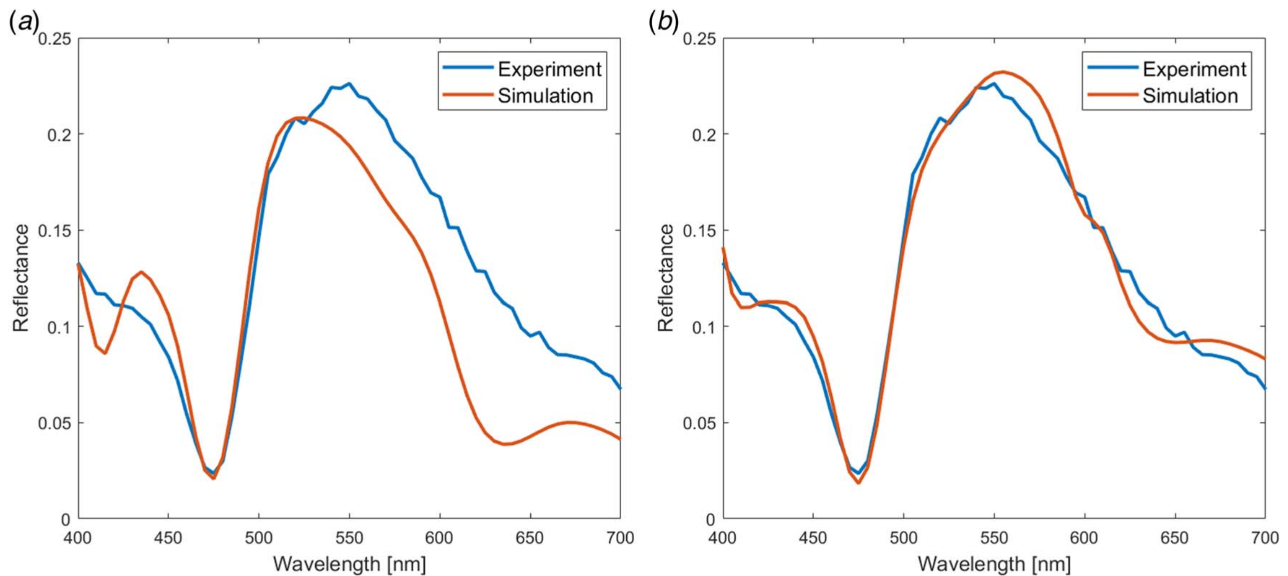

Fig. 5 (*a*) An example of the best matching reflectance spectrum obtained using only the initial library of simulated reflectance spectra. (*b*) The best matching reflectance spectrum for the same experimental reflectance spectrum show in (*a*), but this time obtained using the newly proposed inverse problem-based optimization.

Table 1 Results of CD measurement of the designated area in Fig. 3 utilizing (a) optical metrology based on only the best match from the initial library of reflectance spectra, (b) optical metrology utilizing the newly proposed approach based on the inverse problem optimization, (c) mean value of SEM-based measurements of CDs, and (d) standard deviation of SEM-based measurements of CDs

Critical dimension (nm)	A	B	C	D	E	F	H	P
(a) Initial library only	160	110	121	121	300	350	375	200
(b) Inverse problem-based result	165.2	108.1	117	117	304.8	349.6	409.5	200
(c) SEM measurements—mean	166	107	116	116	312	356	414	200
(d) SEM measurements—St. Dev.	2	2	1	1	3	2	1	0

Table 2 Illustration of measurement time required to measure a full 300 mm wafer with hourglass pattern using different (microscopy or optical) metrology methods

Methods	Experimental gathering of measurements	Library generation	CD inference
Scanning electron microscopy	~ 100 days	0	0
Atomic force microscopy	~800 days	0	0
Point-to-point scatterometry	20 h	>60 years	~3.5 years
Imaging-based scatterometry	5.4 min	>60 years	~3.5 years
Imaging-based scatterometry with efficient search	5.4 min	>60 years	~4 months
Newly proposed optical metrology method using inverse problems	5.4 min	10 Days	3 days

problem-based procedure described in this article resulted in very similar CD measurements compared to the SEM-based inspection. The number of inverse problem iterations gradually went down as inverse problems were solved for more and more reflectance spectra from the field of view of the inspection device, leading to addition of new simulations into the library. Ultimately, toward the end of the inspection process, the library became rich enough that no inverse problem was needed, and the best matches identified from the library already satisfied the convergence condition for most of the pixels.

In order to analyze the speed of the proposed method, we evaluated and compared times needed to measure a full 300 mm wafer utilizing SEM, point-to-point scatterometry, imaging-based scatterometry, and the inverse problem-based optical metrology method introduced in this article. Table 2 summarizes the results of this analysis and clearly shows that the newly proposed method enables significantly faster inspection compared to other methods. Let us emphasize that the CD inspection using the newly proposed inverse problem-based procedure can be dramatically parallelized since determination of CDs from reflectance spectra acquired by each pixel in the field of view of the inspection device can be treated completely independently.

Finally, we evaluated the Gage R&R ratio for the proposed metrology and compared it to that of the SEM-based inspection method, which is generally considered as the most accurate, though also perhaps one of the slowest approaches to inspecting nanopatterns. Average CD measurements, as well as Gage R&R ratios for all eight CDs, are shown in Table 3. One can clearly observe that the newly proposed method obtained accurate CD measurements, without deteriorating the Gage R&R ratios (even improving it for five CDs) when compared with the SEM method.[19] Please note that the raw data used for evaluating Gage R&R ratios are provided in the Appendix.

[19]As recommended in Ref. [28], Gage R&R ratios smaller than 10% are considered, Gage R&R ratios between 10% and 30% are considered acceptable though not ideal, and Gage R&R ratios above 30% indicate that the corresponding measurement process is not adequate for the underlying metrology task.

Downloaded from http://nuclearengineering.asmedigitalcollection.asme.org/manufacturingscience/article-pdf/145/6/061010/6995189/manu_145_6_061010.pdf by guest on 16 August 2024

Table 3 CD measurements and Gage R&R evaluation for SEM as well as the proposed optical metrology using inverse problems

	Average CD measurements		Gage R&R ratio (%)	
CD	SEM	Inverse problem	SEM	Inverse problem
A	166.4 nm	164.9 nm	9.8238	12.2114
B	107.3 nm	107.9 nm	12.7276	9.8831
C	116.2 nm	116.9 nm	9.7738	12.4635
D	116.3 nm	116.9 nm	11.3016	10.4748
E	312.8 nm	303.4 nm	13.5008	7.4127
F	356.3 nm	350.7 nm	12.9263	4.4057
H	414.0 nm	409.4 nm	9.0500	12.5007
P	200.1 nm	200.1 nm	11.7416	10.6258

4 Conclusion and Future Work

In this article, optical inspection of CDs of nanopatterned surfaces using reflectance spectra was addressed through the use of an inverse problem-based methodology. Specifically, for each physically measured reflectance spectrum, an inverse problem-based optimization process was formulated to obtain a simulated spectrum that allows for sufficiently accurate estimates of the CDs characterizing the inspected nanopattern geometries. Capabilities of the newly proposed approach were evaluated utilizing semiconductor wafer samples with hourglass patterns characterized by eight CDs. It was observed that one can obtain significantly faster CD measurements compared to inspection times associated with SEM, while at the same time maintaining the Gage R&R levels associated with SEM-based inspection. In conclusion, this method enables dramatically faster and yet accurate and reliable metrology of CDs of large-area nanopatterned surfaces with complex nanostructure arrays.

A clear avenue for extension of this research is to apply the proposed inspection methodology into semiconductor wafers with even more complicated nanostructured patterns, such as wafers with the gate-all-around transistor structures [64]. Another direction for future research could be the use of surrogate models to create an initial library and utilizing ML-based methods to solve inverse problems needed to estimate the CDs associated with inspected nanopatterns. Such an approach would rely on building ML models, such as artificial neural networks, to relate simulated or experimentally gathered reflectance spectra with actual CD measurements obtained via SEM, and then utilizing those models to rapidly estimate CDs based on the newly gathered reflectance spectra.

Acknowledgment

This work was supported in part by the National Science Foundation (NSF) (Cooperative Agreement No. EEC-1160494). This work was also supported in part by a donation from The MathWorks, Inc. to the University of Texas at Austin. Any opinions, findings, conclusions, or recommendations expressed in this article are those of the authors and do not necessarily reflect the views of the NSF or the MathWorks, Inc.

Conflict of Interest

There are no conflicts of interest.

Data Availability Statement

The datasets generated and supporting the findings of this article are obtainable from the corresponding author upon reasonable request.

Appendix

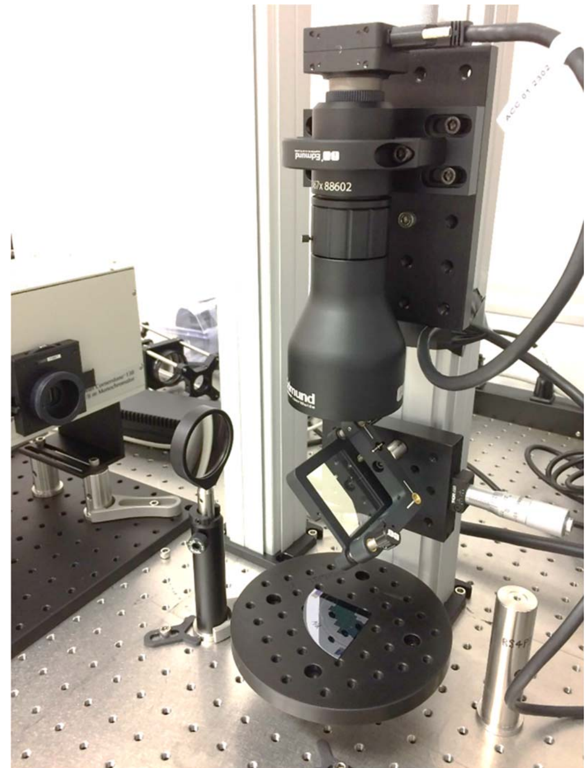

Fig. 6 Hyperspectral imaging system

Experimental measurement of nanostructured wafers is performed utilizing hyperspectral imaging scatterometry metrology system proposed in Ref. [14]. This imaging system (illustrated in Fig. 6) provides field of view of $19 \times 23\ \text{mm}^2$, which allows to take pictures of semiconductor wafer samples using multiple wavelength[20] and simultaneously acquire over 5 million reflectance spectra with respect to those wavelengths. Each reflectance vector represents an area of $10 \times 10\ \mu\text{m}^2$ on the sample and comprises reflectance values obtained for the desired wavelengths, where the reflectance value for each wavelength is calculated as follows:

$$R(\lambda) = \frac{I_{\text{sample}}(\lambda)}{I_{\text{reference}}(\lambda)} \tag{A1}$$

where λ is the wavelength and I is the intensity evaluated as follows:

$$I = (\text{DN} - \text{Noise}_{\text{read}} - \text{Noise}_{\text{dark}}) \times \frac{10^{\frac{\text{Gain}}{10}}}{t_{\text{exp}}} - I_{\text{background}} \tag{A2}$$

where DN stands for digital number (a pixel value in the image), $\text{Noise}_{\text{read}}$ is the read noise of the camera, $\text{Noise}_{\text{dark}}$ is the dark noise of the camera, $I_{\text{background}}$ is the background light intensity in the room, Gain is the camera gain (dB), and t_{exp} is the camera exposure time.

[20]In order to accurately estimate the critical dimensions of nanostructures using the scatterometry-based metrology method, the wavelengths used to simulate reflectance spectra should be exactly the same as wavelengths we utilize to experimentally measure nanostructured wafer samples. In this case, we will set the wavelengths to be from 400 to 700 nm with steps of 5 nm, identical to wavelengths utilized for the reflectance simulation.

Downloaded from http://nuclearengineering.asmedigitalcollection.asme.org/manufacturingscience/article-pdf/145/6/061010/6995189/manu_145_6_061010.pdf by guest on 16 August 2024

Here are the Gage R&R tables for all eight CDs for SEM:

Critical dimension: A						
		Trial number				
Operator	Part	1	2	3	Average	Range
1	1	166.67	166.68	167.04	166.80	0.37
	2	163.65	163.73	163.54	163.64	0.19
	3	169.35	169.70	169.05	169.37	0.65
	4	166.05	165.98	165.45	165.83	0.60
	5	166.67	166.67	167.20	166.85	0.53
2	1	166.24	165.97	166.27	166.16	0.30
	2	163.23	163.76	163.69	163.56	0.53
	3	170.24	170.26	170.61	170.37	0.37
	4	165.79	165.14	165.30	165.41	0.65
	5	166.26	166.36	166.05	166.22	0.31
Metrics	σ_e	σ_o	σ'_o	σ_m	σ_p	Gage R&R
Values	0.2658	0.1336	0.0110	0.2660	2.6949	9.8238

Critical dimension: B						
		Trial number				
Operator	Part	1	2	3	Average	Range
1	1	109.54	109.36	109.53	109.48	0.18
	2	107.63	107.94	107.34	107.64	0.60
	3	106.65	107.24	107.24	107.04	0.59
	4	106.27	106.35	106.73	106.45	0.46
	5	105.28	105.98	105.37	105.54	0.70
2	1	109.53	109.54	109.26	109.44	0.28
	2	109.29	109.41	109.53	109.41	0.24
	3	107.32	107.05	107.15	107.17	0.27
	4	105.27	105.41	105.32	105.33	0.14
	5	105.53	105.56	105.37	105.49	0.19
Metrics	σ_e	σ_o	σ'_o	σ_m	σ_p	Gage R&R
Values	0.2156	0.1235	0.0298	0.2176	1.6961	12.7276

Critical dimension: C						
		Trial number				
Operator	Part	1	2	3	Average	Range
1	1	118.43	118.57	118.34	118.45	0.23
	2	116.03	116.24	116.13	116.13	0.21
	3	116.41	116.74	116.12	116.42	0.62
	4	112.32	112.05	112.00	112.12	0.32
	5	118.42	118.33	118.37	118.37	0.09
2	1	118.51	118.35	118.59	118.48	0.24
	2	116.00	115.92	116.24	116.05	0.32
	3	116.42	116.55	116.76	116.58	0.34
	4	113.21	112.54	112.98	112.91	0.67
	5	117.16	116.32	116.28	116.59	0.88
Metrics	σ_e	σ_o	σ'_o	σ_m	σ_p	Gage R&R
Values	0.2315	0.1578	0.0973	0.2512	2.5573	9.7738

Critical dimension: D						
		Trial number				
Operator	Part	1	2	3	Average	Range
1	1	118.65	118.37	118.28	118.43	0.37
	2	116.25	116.83	116.25	116.44	0.58
	3	116.35	116.83	116.03	116.40	0.80
	4	112.27	111.95	112.24	112.15	0.32
	5	118.40	118.37	118.41	118.39	0.04
2	1	118.62	118.35	118.93	118.63	0.58
	2	115.94	116.38	116.74	116.35	0.80
	3	116.23	116.76	116.52	116.50	0.53
	4	112.50	112.72	112.84	112.69	0.34
	5	116.70	117.14	116.54	116.79	0.60
Metrics	σ_e	σ_o	σ'_o	σ_m	σ_p	Gage R&R
Values	0.2930	0.1519	0.0595	0.2990	2.6283	11.3016

Critical dimension: E						
		Trial number				
Operator	Part	1	2	3	Average	Range
1	1	314.24	314.05	314.53	314.27	0.48
	2	312.72	312.86	312.43	312.67	0.43
	3	313.53	313.26	313.02	313.27	0.51
	4	313.64	313.15	313.16	313.32	0.49
	5	309.87	309.87	309.76	309.83	0.11
2	1	315.24	315.35	315.26	315.28	0.11
	2	312.26	312.68	312.53	312.49	0.42
	3	313.20	313.73	313.28	313.40	0.53
	4	313.25	313.53	313.40	313.39	0.28
	5	310.04	309.35	310.24	309.88	0.89
Metrics	σ_e	σ_o	σ'_o	σ_m	σ_p	Gage R&R
Values	0.2510	0.1921	0.1420	0.2884	2.1167	13.5008

Critical dimension: F						
		Trial number				
Operator	Part	1	2	3	Average	Range
1	1	358.50	358.75	358.25	358.50	0.50
	2	358.53	358.74	358.15	358.47	0.59
	3	357.23	357.65	357.15	357.34	0.50
	4	354.27	354.75	354.26	354.43	0.49
	5	352.64	352.35	352.54	352.51	0.29
2	1	358.34	357.97	358.46	358.26	0.49
	2	358.69	357.32	358.62	358.21	1.37
	3	357.46	357.65	357.85	357.65	0.39
	4	355.27	355.78	355.28	355.44	0.51
	5	352.78	352.45	352.36	352.53	0.42
Metrics	σ_e	σ_o	σ'_o	σ_m	σ_p	Gage R&R
Values	0.3278	0.1489	0.0181	0.3283	2.5186	12.9263

Downloaded from http://nuclearengineering.asmedigitalcollection.asme.org/manufacturingscience/article-pdf/145/6/061010/6995189/manu_145_6_061010.pdf by guest on 16 August 2024

Critical dimension: H						
		Trial number				
Operator	Part	1	2	3	Average	Range
1	1	421.25	420.78	421.67	421.23	0.89
	2	414.31	414.35	414.12	414.26	0.23
	3	415.90	415.89	415.24	415.68	0.66
	4	408.29	408.68	408.45	408.47	0.39
	5	411.11	411.13	410.87	411.04	0.26
2	1	420.41	420.51	420.37	420.43	0.14
	2	415.32	414.76	414.65	414.91	0.67
	3	415.23	414.72	415.14	415.03	0.51
	4	409.53	408.82	408.34	408.90	1.19
	5	410.54	410.24	408.54	409.77	2.00
Metrics	σ_e	σ_o	σ'_o	σ_m	σ_p	Gage R&R
Values	0.4097	0.2910	0.2395	0.4746	5.2224	9.0500

Critical dimension: P						
		Trial number				
Operator	Part	1	2	3	Average	Range
1	1	201.59	201.05	201.24	201.42	0.35
	2	200.18	200.34	200.00	200.17	0.34
	3	199.43	200.00	200.00	199.81	0.57
	4	200.08	200.14	200.00	200.07	0.14
	5	199.14	199.08	198.41	198.88	0.73
2	1	201.40	201.63	201.08	201.37	0.55
	2	200.00	200.62	200.41	200.34	0.62
	3	200.32	200.13	200.67	200.37	0.54
	4	200.12	200.00	200.00	200.04	0.12
	5	198.85	198.34	198.73	198.64	0.51
Metrics	σ_e	σ_o	σ'_o	σ_m	σ_p	Gage R&R
Values	0.2640	0.1594	0.0883	0.2784	2.3546	11.7416

Here are the Gage R&R tables for all eight CDs evaluated for the proposed optical metrology method:

CD: A						
		Trial number				
Operator	Part	1	2	3	Average	Range
1	1	164.10	164.10	164.20	164.13	0.10
	2	165.20	165.20	165.10	165.17	0.10
	3	165.00	165.00	165.10	165.03	0.10
	4	164.90	164.90	164.80	164.87	0.10
	5	165.20	165.30	165.10	165.20	0.20
2	1	164.00	164.00	164.00	164.00	0.00
	2	165.20	165.10	165.00	165.10	0.20
	3	165.10	165.20	165.20	165.17	0.10
	4	165.10	165.10	165.10	165.10	0.00
	5	165.10	165.20	165.20	165.17	0.10
Metrics	σ_e	σ_o	σ'_o	σ_m	σ_p	Gage R&R
Values	0.0591	0.0236	0.0000	0.0591	0.4801	12.2114

CD: C						
		Trial number				
Operator	Part	1	2	3	Average	Range
1	1	117.20	117.20	117.30	117.23	0.10
	2	117.00	117.10	117.00	117.03	0.10
	3	115.30	115.40	115.30	115.33	0.10
	4	117.40	117.20	117.20	117.27	0.20
	5	117.20	117.20	117.30	117.23	0.10
2	1	117.40	117.20	117.30	117.30	0.20
	2	117.20	117.30	117.30	117.27	0.10
	3	115.80	115.50	115.60	115.63	0.30
	4	117.50	117.30	117.30	117.37	0.20
	5	117.00	117.00	117.10	117.03	0.10
Metrics	σ_e	σ_o	σ'_o	σ_m	σ_p	Gage R&R
Values	0.0886	0.0887	0.0442	0.0990	0.7882	12.4635

CD: B						
		Trial number				
Operator	Part	1	2	3	Average	Range
1	1	108.30	108.30	108.40	108.33	0.10
	2	108.10	108.00	108.10	108.07	0.10
	3	106.70	106.80	106.80	106.77	0.10
	4	108.00	107.90	107.90	107.93	0.10
	5	108.20	108.20	108.20	108.20	0.00
2	1	108.20	108.20	108.30	108.23	0.10
	2	108.00	108.00	108.00	108.00	0.00
	3	107.00	107.00	107.10	107.03	0.10
	4	108.10	108.20	108.00	108.10	0.20
	5	108.20	108.10	108.00	108.10	0.20
Metrics	σ_e	σ_o	σ'_o	σ_m	σ_p	Gage R&R
Values	0.0591	0.0296	0.0000	0.0591	0.5947	9.8831

CD: D						
		Trial number				
Operator	Part	1	2	3	Average	Range
1	1	117.20	117.20	117.30	117.23	0.10
	2	117.00	117.10	117.00	117.03	0.10
	3	115.30	115.40	115.30	115.33	0.10
	4	117.40	117.20	117.20	117.27	0.20
	5	117.20	117.20	117.30	117.23	0.10
2	1	117.40	117.20	117.30	117.30	0.20
	2	117.30	117.30	117.30	117.30	0.00
	3	115.60	115.50	115.60	115.57	0.10
	4	117.50	117.30	117.30	117.37	0.20
	5	117.00	117.00	117.10	117.03	0.10
Metrics	σ_e	σ_o	σ'_o	σ_m	σ_p	Gage R&R
Values	0.0709	0.0827	0.0461	0.0845	0.8025	10.4748

Downloaded from http://nuclearengineering.asmedigitalcollection.asme.org/manufacturingscience/article-pdf/145/6/061010/6995189/manu_145_6_061010.pdf by guest on 16 August 2024

CD: E						
		Trial number				
Operator	Part	1	2	3	Average	Range
1	1	233.20	233.10	233.00	233.10	0.20
	2	232.80	232.90	233.00	232.90	0.20
	3	230.30	230.10	230.20	230.20	0.20
	4	233.30	233.30	233.40	233.33	0.10
	5	232.90	232.90	233.00	232.93	0.10
2	1	233.40	233.40	233.50	233.43	0.10
	2	233.00	233.10	233.10	233.07	0.10
	3	229.40	229.60	229.40	229.47	0.20
	4	233.00	232.80	232.80	232.87	0.20
	5	233.10	233.10	233.00	233.07	0.10
Metrics	σ_e	σ_o	σ'_o	σ_m	σ_p	Gage R&R
Values	0.0886	0.1005	0.0647	0.1097	1.4761	7.4127

CD: H						
		Trial number				
Operator	Part	1	2	3	Average	Range
1	1	410.50	410.40	410.40	410.43	0.10
	2	410.50	410.50	410.50	410.50	0.00
	3	404.80	404.60	404.40	404.60	0.40
	4	410.50	410.50	410.40	410.47	0.10
	5	410.30	410.50	410.30	410.37	0.20
2	1	410.20	410.10	410.20	410.17	0.10
	2	410.30	410.30	410.30	410.30	0.00
	3	406.30	406.10	406.10	406.17	0.20
	4	411.00	411.00	410.70	410.90	0.30
	5	410.40	410.50	410.40	410.43	0.10
Metrics	σ_e	σ_o	σ'_o	σ_m	σ_p	Gage R&R
Values	0.0886	0.2837	0.2731	0.2871	2.2786	12.5007

CD: F						
		Trial number				
Operator	Part	1	2	3	Average	Range
1	1	318.30	318.50	318.50	318.43	0.20
	2	318.60	318.50	318.60	318.57	0.10
	3	314.70	314.70	314.80	314.73	0.10
	4	318.80	318.80	318.70	318.77	0.10
	5	318.30	318.20	318.20	318.23	0.10
2	1	318.40	318.50	318.40	318.43	0.10
	2	318.50	318.70	318.70	318.63	0.20
	3	314.40	314.50	314.40	314.43	0.10
	4	318.50	318.60	318.40	318.50	0.20
	5	318.40	318.40	318.50	318.43	0.10
Metrics	σ_e	σ_o	σ'_o	σ_m	σ_p	Gage R&R
Values	0.0768	0.0532	0.0000	0.0768	1.7412	4.4057

CD: P						
		Trial number				
Operator	Part	1	2	3	Average	Range
1	1	201.59	20.1.05	201.24	201.42	0.35
	2	200.18	200.34	200.00	200.17	0.34
	3	199.43	200.00	200.00	199.81	0.57
	4	200.08	200.14	200.00	200.07	0.14
	5	199.14	199.08	198.41	198.88	0.73
2	1	201.40	201.63	201.08	201.37	0.55
	2	200.00	200.00	200.41	200.14	0.41
	3	200.32	200.13	200.67	200.37	0.54
	4	200.12	200.00	200.00	200.04	0.12
	5	198.85	198.34	198.73	198.64	0.51
Metrics	σ_e	σ_o	σ'_o	σ_m	σ_p	Gage R&R
Values	0.2516	0.1227	0.0000	0.2516	2.3546	10.6258

References

[1] Chen, W. T., Zhu, A. Y., Sanjeev, V., Khorasaninejad, M., Shi, Z., Lee, E., and Capasso, F., 2018, "A Broadband Achromatic Metalens for Focusing and Imaging in the Visible," Nat. Nanotechnol., **13**(3), pp. 220–226.

[2] Moitra, P., Slovick, B. A., Li, W., Kravchencko, I. I., Briggs, D. P., Krishnamurthy, S., and Valentine, J., 2015, "Large-scale all-Dielectric Metamaterial Perfect Reflectors," ACS Photon., **2**(6), pp. 692–698.

[3] Wang, W.-C., Lin, C.-W., Chen, H.-J., Chang, C.-W., Huang, J.-J., Yang, M.-J., Tjahjono, B., Huang, J.-J., Hsu, W.-C., and Chen, M.-J., 2013, "Surface Passivation of Efficient Nanotextured Black Silicon Solar Cells Using Thermal Atomic Layer Deposition," ACS Appl. Mater Interfaces, **5**(19), pp. 9752–9759.

[4] Sreenivasan, S. V., 2017, "Nanoimprint Lithography Steppers for Volume Fabrication of Leading-Edge Semiconductor Integrated Circuits," Microsyst. Nanoeng., **3**(1), pp. 1–19.

[5] Ahn, S. H., Yang, S., Miller, M., Ganapathisubramanian, M., Menezes, M., Choi, J. H., Xu, F. Y., Resnick, D. J., and Sreenivasan, S. v., 2013, "High-performance Wire-Grid Polarizers Using jet and Flash^{TM} Imprint Lithography," J. Micro/Nanolith. MEMS. MOEMS., **12**(3), p. 31104.

[6] Catrysse, P. B., and Fan, S., 2010, "Nanopatterned Metallic Films for use as Transparent Conductive Electrodes in Optoelectronic Devices," Nano Lett., **10**(8), pp. 2944–2949.

[7] Proust, J., Bedu, F., Gallas, B., Ozerov, I., and Bonod, N., 2016, "All-Dielectric Colored Metasurfaces With Silicon Mie Resonators," ACS Nano., **10**(8), pp. 7761–7767.

[8] Boden, S. A., and Bagnall, D. M., 2010, "Optimization of Moth-Eye Antireflection Schemes for Silicon Solar Cells," Prog. Photovolt. Res. Appl., **18**(3), pp. 195–203.

[9] Yeap, Y. M., Geddada, N., and Ukil, A., 2018, "Capacitive Discharge Based Transient Analysis With Fault Detection Methodology in dc System," Int. J. Electr. Power Energy Syst., **97**, pp. 127–137.

[10] Park, H., Dan, Y., Seo, K., Yu, Y. J., Duane, P. K., Wober, M., and Crozier, K. B., 2014, "Filter-Free Image Sensor Pixels Comprising Silicon Nanowires With Selective Color Absorption," Nano Lett., **14**(4), pp. 1804–1809.

[11] Na, H., and Endoh, T., 2013, "A Multi-Pillar Vertical Metal–Oxide–Semiconductor Field-Effect Transistor Type Dynamic Random Access Memory Core Circuit for Sub-1 V Core Voltage Operation Without Overdrive Technique," Jpn. J. Appl. Phys., **52**(4S), p. 04C. E08.

[12] McMullan, D., 1995, "Scanning Electron Microscopy 1928–1965," Scanning, **17**(3), pp. 175–185.

[13] Rugar, D., and Hansma, P., 1990, "Atomic Force Microscopy," Phys. Today, **43**(10), pp. 23–30.

[14] Gawlik, B., Barrera, C., Edward, T. Y., and v Sreenivasan, S., 2020, "Hyperspectral Imaging for High-Throughput, Spatially Resolved Spectroscopic Scatterometry of Silicon Nanopillar Arrays," Opt. Exp., **28**(10), pp. 14209–14221.

[15] Marroquin, M., Bruce, T., Pellegrino, J., Wickramasinghe, S. R., and Husson, S. M., 2011, "Characterization of Asymmetry in Microporous Membranes by Cross-Sectional Confocal Laser Scanning Microscopy," J. Memb. Sci., **379**(1–2), pp. 504–515.

[16] Faria-Briceno, J. J., Sasidharan, V., Neumann, A., Singhal, S., v Sreenivasan, S., and Brueck, S. R. J., 2021, "High-Speed In-Line Optical Angular Scatterometer for High-Throughput Roll-to-Roll Nanofabrication," Novel Patterning Technologies 2021, California, Feb. 22–27, p. 116100F.

[17] Faria-Briceno, J. J., Zhu, R., Sasidharan, V., Neumann, A., Singhal, S., Sreenivasan, S. v., and Brueck, S. R. J., 2019, "Optical Angular Scatterometry: In-Line Metrology Approach for Roll-to-Roll and Nanoimprint Fabrication," J. Vac. Sci. Technol., B: Nanotechnol. Microelectron.: Mater., Process., Meas., Phenom., **37**, p. 52904.

[18] Zhu, R., Faria-Briceno, J. J., Brueck, S. R. J., Joseph, P., Singhal, S., and Sreenivasan, V. S., 2020, "Nanoscale Limits of Angular Optical Scatterometry," AIP Adv., **10**(1), p. 15140.

[19] Madsen, M. H., and Hansen, P.-E., 2016, "Imaging Scatterometry for Flexible Measurements of Patterned Areas," Opt. Exp., **24**(2), pp. 1109–1117.

[20] Raymond, C., 2005, "Overview of Scatterometry Applications in High Volume Silicon Manufacturing," AIP Conference Proceedings, Richardson, TX, Mar. 15–18, pp. 394–402.

[21] Moharam, M. G., and Gaylord, T. K., 1981, "Rigorous Coupled-Wave Analysis of Planar-Grating Diffraction," JOSA, **71**(7), pp. 811–818.

[22] Taflove, A., and Hagness, S. C., 2005, *Computational Electrodynamics: The Finite-Difference Time-Domain Method*, Elsevier, Burlington, MA.

[23] Sabbagh, R., Živković, S., Gawlik, B., Sreenivasan, S. v., Stothert, A., Majstorovic, V., and Djurdjanovic, D., 2022, "Organization of Big Metrology

Downloaded from http://nuclearengineering.asmedigitalcollection.asme.org/manufacturingscience/article-pdf/145/6/061010/6995189/manu_145_6_061010.pdf by guest on 16 August 2024

Data Within the Cyber-Physical Manufacturing Metrology Model (CPM3)," CIRP J. Manuf. Sci. Technol., **36**, pp. 90–99.
[24] Sabbagh, R., Gawlik, B., Sreenivasan, S. V., Stothert, A., Majstorovic, V., and Djurdjanovic, D., 2020, "Big Data Curation for Analytics Within the Cyber-Physical Manufacturing Metrology Model (CPM^3)," Procedia CIRP, **93**, pp. 491–495.
[25] Kohonen, T., 1990, "Self-Organizing Map," Proc. IEEE, **78**(9), pp. 1464–1480.
[26] Aremu, O. O., Salvador Palau, A., Hyland-Wood, D., Parlikad, A. K., and McAree, P. R., 2018, "Structuring Data for Intelligent Predictive Maintenance in Asset Management," 16th IFAC Symposium on Information Control Problems in Manufacturing, Bergamo, Italy, June 11–13.
[27] Bhattacharya, A., 2014, *Fundamentals of Database Indexing and Searching*, CRC Press, Boca Raton, FL.
[28] Zanobini, A., Sereni, B., Catelani, M., and Ciani, L., 2016, "Repeatability and Reproducibility Techniques for the Analysis of Measurement Systems," Measurement, **86**, pp. 125–132.
[29] Tarantola, A., 2005, *Inverse Problem Theory and Methods for Model Parameter Estimation*, Society for Industrial and Applied Mathematics, Philadelphia, PA.
[30] Aster, R. C., Borchers, B., and Thurber, C. H., 2018, *Parameter Estimation and Inverse Problems*, Elsevier, New York.
[31] Biegler, L., Biros, G., Ghattas, O., Heinkenschloss, M., Keyes, D., Mallick, B., Marzouk, Y., Tenorio, L., van Bloemen Waanders, B., and Willcox, K., 2011, *Large-Scale Inverse Problems and Quantification of Uncertainty*, John Wiley & Sons Ltd, Chichester, UK.
[32] Bui-Thanh, T., Ghattas, O., Martin, J., and Stadler, G., 2013, "A Computational Framework for Infinite-Dimensional Bayesian Inverse Problems Part I: The Linearized Case, With Application to Global Seismic Inversion," SIAM J. Sci. Comput., **35**(6), pp. A2494–A2523.
[33] Petra, N., Martin, J., Stadler, G., and Ghattas, O., 2014, "A Computational Framework for Infinite-Dimensional Bayesian Inverse Problems, Part II: Stochastic Newton MCMC With Application to Ice Sheet Flow Inverse Problems," SIAM J. Sci. Comput., **36**(4), pp. A1525–A1555.
[34] Judd, K., 2008, "Forecasting With Imperfect Models, Dynamically Constrained Inverse Problems, and Gradient Descent Algorithms," Phys. D., **237**(2), pp. 216–232.
[35] Thacker, W. C., 1992, "Oceanographic Inverse Problems," Phys. D, **60**(1–4), pp. 16–37.
[36] Bertero, M., Boccacci, P., and de Mol, C., 2021, *Introduction to Inverse Problems in Imaging*, CRC Press, Boca Raton, FL.
[37] Seo, J. K., and Woo, E. J., 2012, *Nonlinear Inverse Problems in Imaging*, John Wiley & Sons, Chichester, UK.
[38] Karwowski, J., 2009, "Inverse Problems in Quantum Chemistry," Int. J. Quantum Chem., **109**(11), pp. 2456–2463.
[39] Li, X., Li, Z., and Wang, L., 2003, "The Inverse Problems for Some Topological Indices in Combinatorial Chemistry," J. Comput. Biol., **10**(1), pp. 47–55.
[40] Engl, H. W., Flamm, C., Kügler, P., Lu, J., Müller, S., and Schuster, P., 2009, "Inverse Problems in Systems Biology," Inverse Probl., **25**(12), p. 123014.
[41] Forssén, P., Arnell, R., and Fornstedt, T., 2006, "An Improved Algorithm for Solving Inverse Problems in Liquid Chromatography," Comput. Chem. Eng., **30**(9), pp. 1381–1391.
[42] de Vito, E., Rosasco, L., Caponnetto, A., de Giovannini, U., Odone, F., and Bartlett, P., 2005, "Learning From Examples as an Inverse Problem," J. Mach. Learn. Res., **6**(5), pp. 883–904.
[43] Prato, M., and Zanni, L., 2008, "Inverse Problems in Machine Learning: An Application to Brain Activity Interpretation," J. Phys. Conf. Ser., 135(1), p. 12085.
[44] Mohamad-Djafari, A., 2013, *Inverse Problems in Vision and 3D Tomography*, John Wiley & Sons, Hoboken, NJ.
[45] Jones, A. G., and Taylor, C. J., 1994, "Solving Inverse Problems in Computer Vision by Scale Space Reconstruction, MVA," pp. 401–404.
[46] Zaoui, A., Menana, H., Feliachi, M., and Berthiau, G., 2010, "Inverse Problem in Nondestructive Testing Using Arrayed Eddy Current Sensors," Sensors, **10**(9), pp. 8696–8704.
[47] Fleisch, D., 2008, *A Student's Guide to Maxwell's Equations*, Cambridge University Press, Cambridge, UK.
[48] Strikwerda, J. C., 2004, *Finite Difference Schemes and Partial Differential Equations*, SIAM, Pacific Grove, CA.
[49] Liu, K.-Y., Liu, J., and Herbert, J. M., 2017, "Accuracy of Finite-Difference Harmonic Frequencies in Density Functional Theory," J. Comput. Chem., **38**(19), pp. 1678–1684.
[50] Pardo, D., Matuszyk, P. J., Puzyrev, V., Torres-Verdin, C., Nam, M. J., and Calo, V. M., 2021, *Modeling of Resistivity and Acoustic Borehole Logging Measurements Using Finite Element Methods*, Amsterdam, The Netherlands.
[51] Moré, J. J., and Sorensen, D. C., 1982, "Newton's Method."
[52] Dennis, J. E., Jr., and Moré, J. J., 1977, "Quasi-Newton Methods, Motivation and Theory," SIAM Rev., **19**(1), pp. 46–89.
[53] Greiner, R., 1996, "PALO: A Probabilistic Hill-Climbing Algorithm," Artif. Intell., **84**(1–2), pp. 177–208.
[54] Broyden, C. G., 1969, "A New Double-Rank Minimisation Algorithm. Preliminary Report," Notices of the American Mathematical Society, Providence, RI, Vol. 16, No. 4. p. 670.
[55] Fletcher, R., 1970, "A New Approach to Variable Metric Algorithms," Comput J., **13**(3), pp. 317–322.
[56] Goldfarb, D., 1970, "A Family of Variable-Metric Methods Derived by Variational Means," Math Comput., **24**(109), pp. 23–26.
[57] Shanno, D. F., 1970, "Conditioning of Quasi-Newton Methods for Function Minimization," Math Comput., **24**(111), pp. 647–656.
[58] Saltelli, A., 2002, "Sensitivity Analysis for Importance Assessment," Risk Anal., **22**(3), pp. 579–590.
[59] Woodbury, M. A., 1950, *Inverting Modified Matrices*, Department of Statistics, Princeton, NJ.
[60] Wolfe, P., 1969, "Convergence Conditions for Ascent Methods," SIAM Rev., **11**(2), pp. 226–235.
[61] Postek, M. T., and Vladár, A. E., 2013, "Does Your SEM Really Tell the Truth?—How Would You Know? Part 1, Scanning, **35**(6), pp. 355–361.
[62] Schneider, C. A., Rasband, W. S., and Eliceiri, K. W., 2012, "NIH Image to ImageJ: 25 Years of Image Analysis," Nat. Methods., **9**(7), pp. 671–675.
[63] Lam, A., 2020, "BFGS in a Nutshell: An Introduction to Quasi-Newton Methods, Towards Data Science," https://towardsdatascience.com/bfgs-in-a-nutshell-an-introduction-to-quasi-newton-methods-21b0e13ee504, Accessed January 9, 2022.
[64] Jimenez, D., Saenz, J. J., Iniguez, B., Sune, J., Marsal, L. F., and Pallares, J., 2004, "Modeling of Nanoscale Gate-All-Around MOSFETs," IEEE Electron Dev. Lett., **25**(5), pp. 314–316.
[65] Guyon, I., and Elisseeff, A., 2003, "An Introduction to Variable and Feature Selection," J. Mach. Learn. Res., **3**, pp. 1157–1182.
[66] Cunningham, P., Kathirgamanathan, B., and Delany, S. J., 2021, "Feature Selection Tutorial With Python Examples," ArXiv Preprint ArXiv:2106.06437.
[67] Ronaghan, S., 2018, "The Mathematics of Decision Trees, Random Forest and Feature Importance in Scikit-learn and Spark, Towards Data Science," https://towardsdatascience.com/the-mathematics-of-decision-trees-random-forest-and-feature-importance-in-scikit-learn-and-spark-f2861df67e3, Accessed January 8, 2022.

Downloaded from http://nuclearengineering.asmedigitalcollection.asme.org/manufacturingscience/article-pdf/145/6/061010/6995189/manu_145_6_061010.pdf by guest on 16 August 2024